

# Toward Healthcare Diagnoses by Machine-Learning-Enabled Volatile Organic Compound Identification

Jianxiong Zhu, Zhihao Ren, and Chengkuo Lee\*



Cite This: *ACS Nano* 2021, 15, 894–903



Read Online

ACCESS |



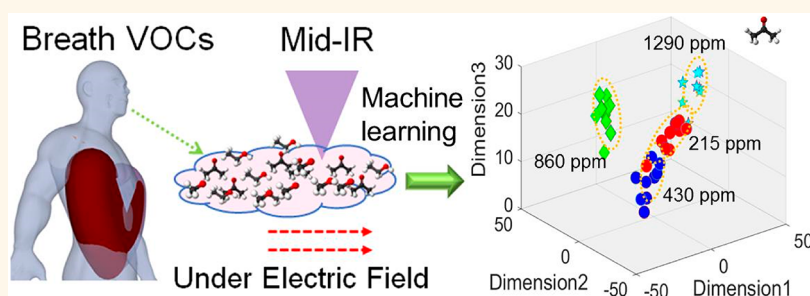
Metrics & More



Article Recommendations



Supporting Information



**ABSTRACT:** As a natural monitor of health conditions for human beings, volatile organic compounds (VOCs) act as significant biomarkers for healthcare monitoring and early stage diagnosis of diseases. Most existing VOC sensors use semiconductors, optics, and electrochemistry, which are only capable of measuring the total concentration of VOCs with slow response, resulting in the lack of selectivity and low efficiency for VOC detection. Infrared (IR) spectroscopy technology provides an effective solution to detect chemical structures of VOC molecules by absorption fingerprints induced by the signature vibration of chemical stretches. However, traditional IR spectroscopy for VOC detection is limited by the weak light–matter interaction, resulting in large optical paths. Leveraging the ultrahigh electric field induced by plasma, the vibration of the molecules is enhanced to improve the light–matter interaction. Herein, we report a plasma-enhanced IR absorption spectroscopy with advantages of fast response, accurate quantization, and good selectivity. An order of  $\sim$ kV voltage was achieved from the multiswitched manipulation of the triboelectric nanogenerator by repeated sliding. The VOC species and their concentrations were well-quantified from the wavelength and intensity of spectra signals with the enhancement from plasma. Furthermore, machine learning has visualized the relationship of different VOCs in the mixture, which demonstrated the feasibility of the VOC identification to mimic patients.

**KEYWORDS:** mid-infrared spectroscopy, healthcare diagnosis, volatile organic compound, machine learning, triboelectric nanogenerator

Volatile organic compounds (VOCs) are a group of chemical compounds that are prone to evaporate under ambient conditions due to high vapor pressure, low boiling point, and strong reactivity.<sup>1–3</sup> VOCs are efficiently emitted as gas-phase molecules by a phase transition from solid and liquid phases. The primary sources of VOCs nowadays are from automobile exhaust, industrial emissions, petroleum refining, solvent evaporation, fossil fuel combustion, and biogenic emissions.<sup>3,4</sup> The significant impacts on humans are the inhalation or exposure to the VOCs' environment, which could induce various acute and chronic health effects, such as central nervous system impairment, cancer, skin irritation, and respiratory-system damage. On the other hand, the measure-

ment of the levels of VOCs from breath reflects the health condition of specific organs to identify the disease of a human being for early healthcare diagnosis. Most existing VOC sensors use methods such as oxide semiconductors and optical and electrochemical methods.<sup>5–16</sup> However, those kinds of VOC sensors are only capable of measuring the total concentration of

**Received:** September 4, 2020

**Accepted:** December 8, 2020

**Published:** December 14, 2020



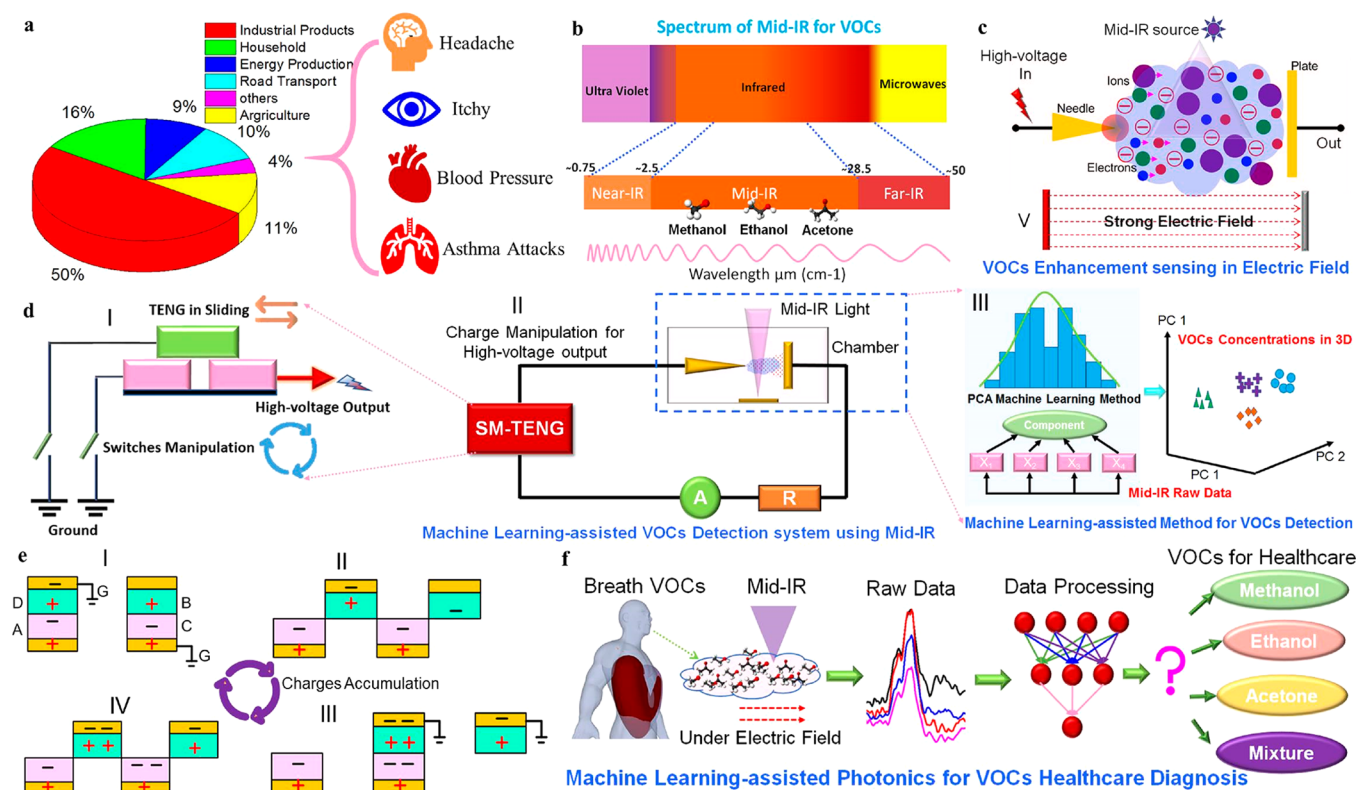


**Figure 1.** Machine-learning-assisted and plasma enhancement mid-IR methodology for VOC healthcare diagnosis. (a) VOC emission distribution and the potential illness to humans. (b) Spectrum of VOCs. (c) VOC detection by the coupling of the strong electric field and the mid-IR. (d) VOC detection by machine-learning-assisted and plasma enhancement mid-IR from a multiswitch manipulation triboelectric nanogenerator (SM-TEG). (e) Working mechanism of the SM-TEG. (h) Machine-learning-assisted and plasma enhancement mid-IR methodology for an early healthcare diagnosis.

VOCs and with slow response, resulting in the lack of selectivity and low efficiency for VOC detection. Thus, the technology that enables good selectivity, fast response, real-time monitoring, and high sensitivity to VOCs is of great importance, especially to early healthcare diagnoses.

To solve the above-mentioned issues, mid-infrared (mid-IR) spectroscopy is considered a feasible solution for VOC detection due to the response of the vibrational modes of molecular bonds in the range 2–25  $\mu\text{m}$ ,<sup>17–19</sup> resulting in absorption and reflection with the intensity of the subsequent infrared beam. Other than the VOC sensors measuring physical properties such as mass, conductivity, density, or viscosity, IR-based VOC sensors detect the chemical properties of molecules by absorption peaks, which reflect the bonding energy of chemical stretches. By retrieving fingerprint absorption in the full mid-IR spectrum, the chemical structures can be reconstructed to distinguish the species of VOC molecules. Additionally, by monitoring the intensity of each absorption peaks, the concentration of specific VOC molecules can be identified through Beer–Lambert’s law, which indicates the linear relationship between concentration and absorbance. However, the vibrational modes of VOC molecules in the mid-IR are weakly coupled to incident IR light, which dramatically constrains the sensing accuracy.<sup>20–22</sup> To improve the sensitivity, the coupling effect between the strong electric field generated by plasma and the molecules provides a way to amplify the IR absorption fingerprint. Therefore, plasma-enhanced infrared absorption (PEIRA) spectroscopy becomes a good candidate for ultrasensitive VOC detection and identification in a mixture

by analyzing absorption fingerprints. Unfortunately, plasma is usually generated by high-voltage direct-current power supplies, which is bulky and power-consuming and does not control the number of charges. The triboelectric nanogenerator (TEG)<sup>23–35</sup> was proposed in 2012 with the advantage of the potential for a high-voltage output based on the coupling of triboelectric and electrostatic induction.<sup>36–47</sup> The TENG microplasma was proposed in 2018. Compared with bulky high-voltage portable power sources for plasma discharge, the concept of this TENG microplasma showed the possibility of the application with advantages of controllable energy output, easy fabrication, and the safe operation.<sup>48–52</sup> Leveraging the tip–plate electrode configuration, the TENG provides an ideal solution to obtain a strong electric field<sup>51–54</sup> to generate plasma for PEIRA application, which could dramatically aid VOC sensing with high sensitivity. Besides, with the trends of fifth-generation cellular network technology (5G),<sup>55–60</sup> machine learning (ML) enables data analytics to be exercised at the cloud server to aid the Internet of Things (IoT).<sup>61–64</sup> Leveraging ML for VOC analysis, real-time dynamic monitoring with fast response and high accuracy can be achieved based on massive spectral data for multiple absorption peaks. The principal component analysis (PCA) in ML provides a feasible solution to enhance the identification accuracy by reinforcing the difference of different data sets from massive spectra for various VOC species and their concentrations.

To realize VOC detection with the advantages of good selectivity, fast response, real-time dynamic monitoring, and high sensitivity, motivated by multiswitch manipulation for a

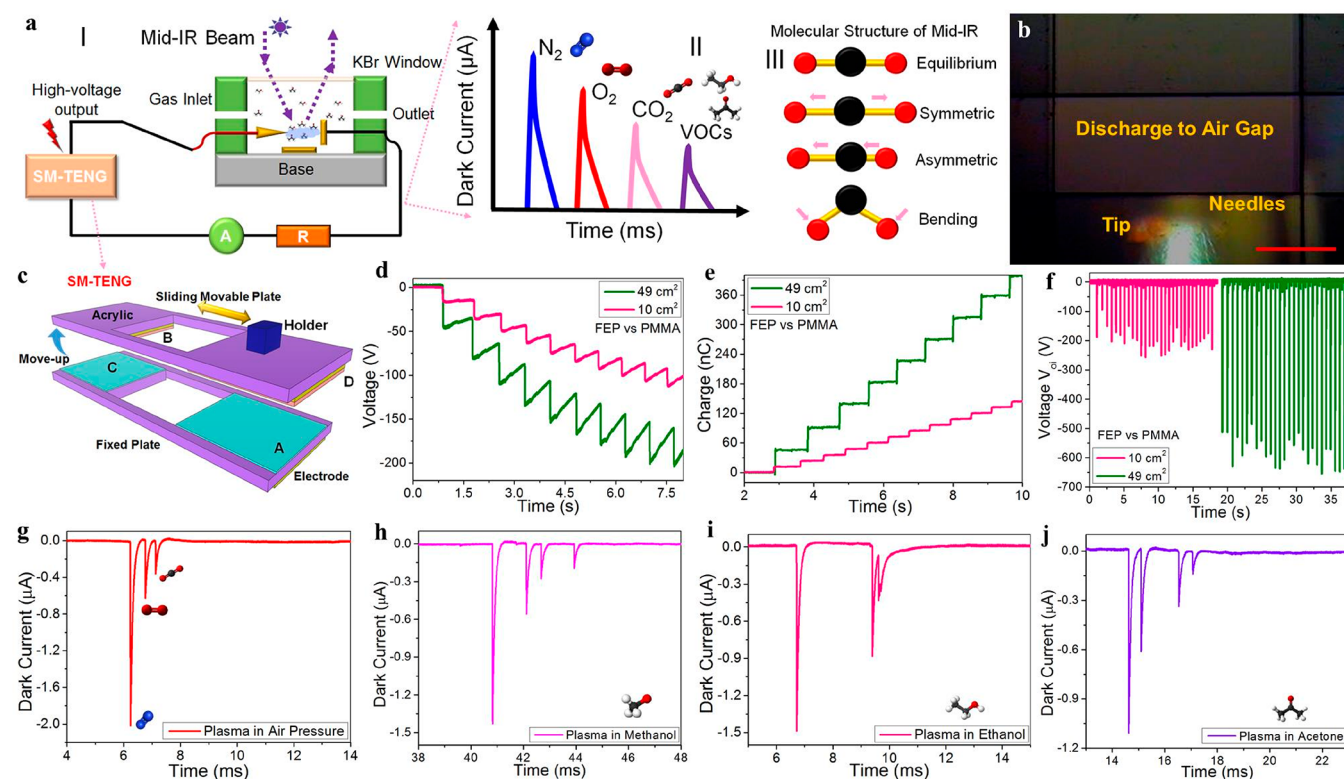


**Figure 2.** Plasma discharge and VOC characteristics. (a) Schematic diagram of plasma discharge enhancement mid-IR for VOC species. (b) Optical image of the needle tip; scale bar 0.5 mm. (c) 3D schematic diagram of the SM-TENG. (d)  $V_{oc}$  from FEP vs PMMA and (e)  $Q_{oc}$ . (f)  $V_{oi}$  from 100 M $\Omega$  oscilloscopes to demonstrate the output voltage from the SM-TENG. (g) Plasma discharge spectrum from the needle–plate electrode configuration under air pressure, (h) in methanol, (i) in ethanol, and (j) in acetone.

high-voltage output, we proposed machine-learning-assisted plasma discharge enhancement of mid-IR for a variety of VOC species detection, such as methanol, ethanol, and acetone. The voltage with the order of  $\sim$ kV was easily achieved from the multiswitched manipulation of a triboelectric nanogenerator (SM-TENG),<sup>65</sup> the output voltage of which is further leveraged in a particular type of tip–plate electrode configuration, making it possible to obtain plasma discharge in a wide range of VOC species. The coupling effect of the strong electric field generated by plasma and mid-IR absorption fingerprints of VOC molecular bonds was demonstrated to enhance VOC sensing and identification. With the aid of PEIRA, a high degree of accuracy of VOC species (methanol, ethanol, and acetone) can be well quantified even in the mixture environment. Furthermore, we demonstrated that the ML-assisted PEIRA could be well visualized the relationship of the different VOC classifications in the sub-ppm concentration level. Finally, the healthcare diagnosis applications of the breath from mimic patients further demonstrated the feasibility of the PEIRA. This work not only shows the possibility of exploring the fundamental phenomenon of plasma–molecule interaction but also presents the feasibility of accurate detection of VOC species for early stage healthcare diagnosis through ML.

## RESULTS AND DISCUSSION

**ML-Assisted PEIRA for VOC Sensing.** Due to the process of industrialization, more and more VOC emissions from various fields have become a serious issue to human healthcare nowadays; for example, the area of industrial products is responsible for almost 50% of all VOC emissions, as shown in Figure 1a.<sup>3,4</sup> Humans' exposure to VOC environment in the

long term might result in severe healthcare problems, such as headaches, itchy eyes, or high blood pressure. To meet the needs of the IoT application for fast and on-site detection of VOC species, the absorption and reflection spectroscopy in the mid-IR could become a solution due to the resonant frequency of the molecular structure of VOCs in a vibrational mode as shown in Figure 1b. Light irradiation is usually classified as mid-IR region (5000–400  $\text{cm}^{-1}$ ), near-IR (10000–4000  $\text{cm}^{-1}$ ), and far-IR (less than 200  $\text{cm}^{-1}$ ). The response of different molecular structures with their vibrational mode in the mid-IR is shown in Figure S1. However, the sensitivity of this VOC sensing does not satisfy the needs of the IoT and early healthcare diagnosis applications, and no report has studied the spectral features of VOCs under the effect of a strong electric field, as shown in Figure 1c. With infrared spectroscopy, the characterizations of all the molecular components were accurately achieved using absorption and reflection in a wide range of VOCs by Fourier-transform infrared spectroscopy (FTIR) equipment. Furthermore, it is assumed that the mid-IR in a strong electric field dramatically affects the sensitivity of the VOC detection due to the high-voltage fluctuation from the plasma discharge onto the vibrational mode of the molecular structure.

Motivated by the logic of the charge accumulation, the SM-TENG was developed to reach a high-voltage output without any external battery. Leveraging the output voltage from the SM-TENG in a special type of tip–plate electrode configuration, machine-learning-assisted plasma enhancement of mid-IR absorption was proposed for an early and fast response to VOCs as shown in Figure 1c. The back and forth sliding and switching operation in time sequence can easily generate a high-voltage output in the SM-TENG, as shown in Figure 1e. The

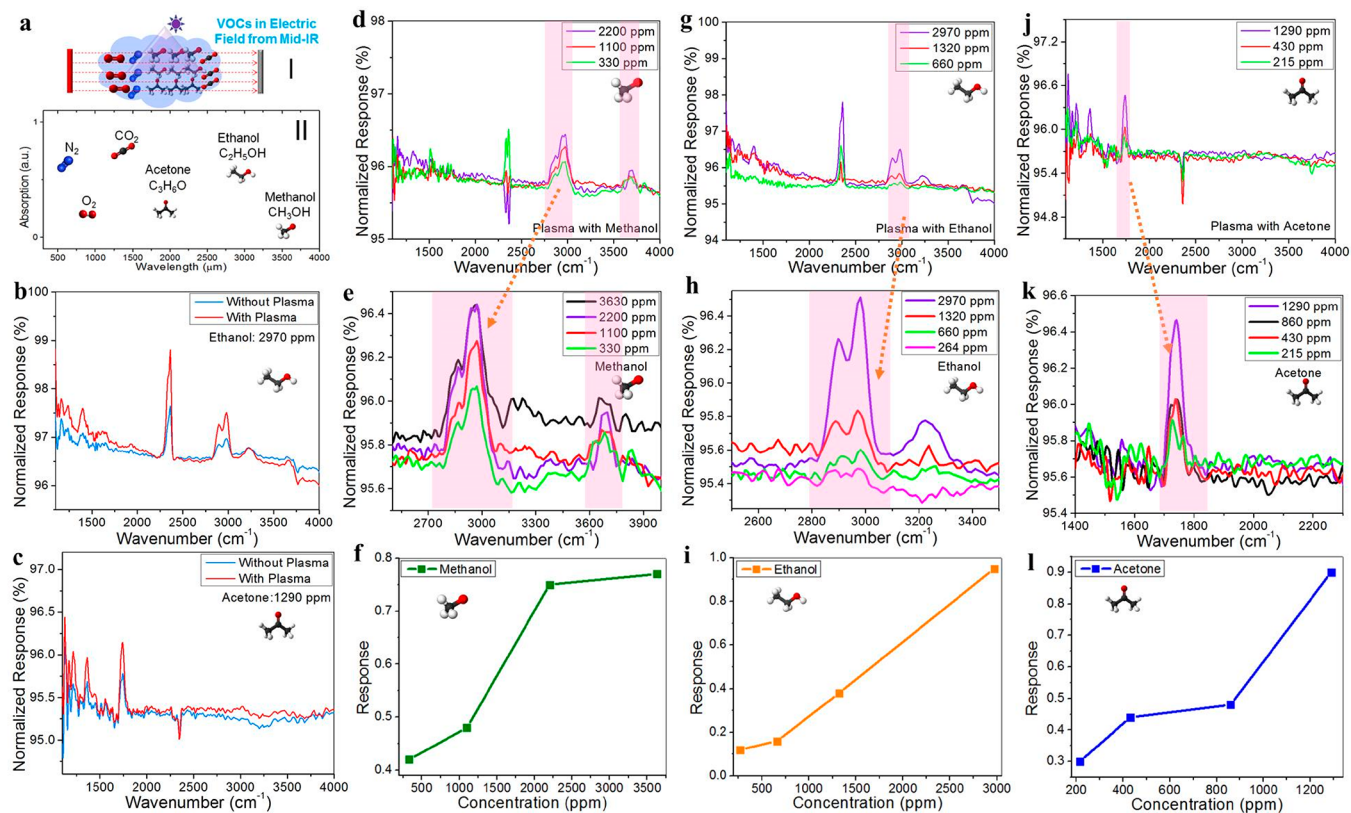


**Figure 3.** Discharge enhancement mid-IR spectrum for VOC detection. (a) Vibrational mode of gas molecules in a strong electric field by mid-IR methodology. (b) Response of the mid-IR to ethanol with/without plasma discharge and (c) to acetone with/without plasma discharge. (d) Response of the mid-IR of different concentrations in methanol with plasma, (e) zoom-in at the range of 2500–4000  $\text{cm}^{-1}$ , and (f) the concentration versus the response of methanol. (g) Response of the mid-IR of different concentrations in ethanol with plasma, (h) zoom-in in the range of 2500–3500  $\text{cm}^{-1}$ , and (i) concentration versus the response of ethanol. (j) Response of the mid-IR of different concentrations in acetone with plasma, (k) zoom-in in the range of 1500–2300  $\text{cm}^{-1}$ , and (l) concentration versus the response of acetone.

initial charges of all the dielectric materials (“A”, “B”, “C”, “D”) are from the triboelectric effect by its friction. The conductive electrodes were located at the backside of all the dielectric materials for charge accumulation (electrode “A” and “B”) from the electrostatic induction by multiswitch operation “on” and “off”. Figure S2 depicts the basic unit for charge generation. Due to the electrostatic effect and the material interface effect, the electrodes of “C” and “D” will obtain charges from the ground, as shown in Figure 1e(I). The function of the multiswitches “off” maintains a separation of charges, as shown in Figure 1e(II)–e(IV), resulting in more charges (“D” and “B”) from the ground for balance. Finally, more charges will accumulate onto the “A” for a high-voltage output. The continuous charge accumulation on dielectric “A” would produce a high-voltage output with more operation cycles. To visualize the relationship of the different VOC species and their concentrations, the PCA algorithm of the machine-learning-assisted method was adopted. As shown in Figure 1f, when a human being is breathing, the VOCs from human breath are detected by the proposed sensing mechanism based on plasma enhancement of the mid-IR. Then the raw data from the FTIR equipment are fed to the machine-learning-assisted computer server for further analysis.

**Characterization of Plasma Generation and VOC Sensing.** The system of the plasma discharge enhancement of the mid-IR for VOC detection is shown in Figure 2a and Video S1. The high voltage was generated from the sliding operation of the SM-TENG, which was leveraged by the needle–plate

electrode configuration for the plasma discharge in the VOC gas chamber. Meanwhile, the mid-IR beam was focused onto the bottom electrode to broaden its response area for the VOC detection in the FTIR equipment. With the coupling effect of the plasma discharge from a particular type of tip–plate electrode configuration and the response of the mid-IR, the high sensitivity of a wide range of VOCs was observed due to the high-voltage fluctuation. With the different motion speeds of the VOCs and gas ions, the drift time to the electrode collector would be present in a pattern due to the fixed weight and volume of the different VOCs, as shown in Figure 2a(II). Due to the different molecule structures and their vibrational modes, as shown in Figure 2a(III), the mid-IR response of the VOCs would be affected in the strong electric field. The optical image of the tip of the needle and discharge is shown in Figure 2b. The 3D schematic diagram of the SM-TENG with a sliding motion is shown in Figure 2c. The sliding mode and the chosen materials in the triboelectric are shown in Figure S3. To investigate the dielectric materials of their electrical performance, different contact areas of similar and different polarity triboelectric materials can be seen in Figure S4. It showed that similar materials resulted in low charge transfer efficiency. It also demonstrated that the device achieves more charges with a larger contact area. The stable output of the open-circuit voltage ( $V_{oc}$ ) and the accumulative open-circuit charges ( $Q_{oc}$ ) was performed, as shown in Figure 2d,e, respectively. The unidirectional flow during the operation dramatically benefited and simplified the system in the plasma discharge. Each step-increase

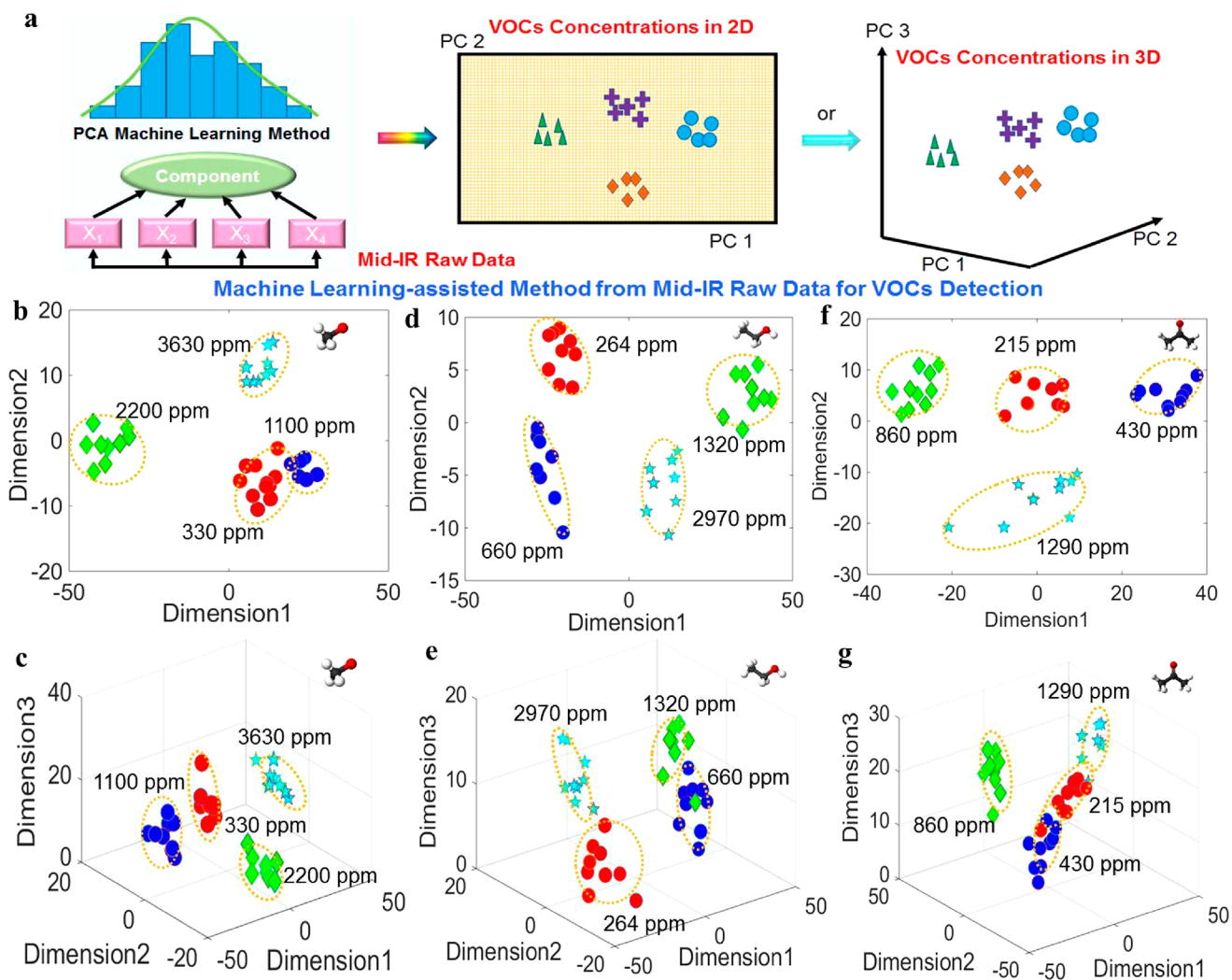


**Figure 4.** Machine-learning-assisted and plasma-enhanced mid-IR methodology for VOC detection. (a) Machine-learning-assisted method for VOCs. (b) Methanol detection in 2D and (c) in 3D. (d) Ethanol detection in 2D and (e) in 3D. (f) Acetone detection in 2D and (g) in 3D.

charge meant a periodic sliding. The output voltage  $V_{oi}$  from the SM-TENG ( $49 \text{ cm}^2$ ) resulted in a 3 times higher voltage than the smallest contact area device ( $10 \text{ cm}^2$ ), as shown in Figure 2f.  $V_{oi}$  was obtained from the resistor (close to the plate side), which was used to evaluate the output energy from the needle–plate configuration by oscilloscope ( $1 \text{ M}\Omega$ ). In an in-depth study of similar materials in the SM-TENG, the results show that similar triboelectric materials induce low charge transfer efficiency and small output voltage, as shown in Figure S5 and Figure S6. Compared with both similar and dissimilar materials in the SM-TENG, the different triboelectric materials have a much higher power transfer efficiency. Thus, the steady discharge output from the electrode “A” would benefit from the air breakdown in an infinite accumulation.

The optical image of the needle–plate electrode configuration is shown in Figure S7a, and the numerical relationships of the output voltage from the different air gaps of the needle–plate electrode configurations are shown in Figure S8. The result shows that the gap of the needle–plate electrode configuration dramatically affects the output voltage. A longer air gap of the needle–plate electrode configuration will induce a smaller output voltage. To demonstrate the status of the discharge in the gas chamber, the dark current patterns of the air pressure are shown in Figure 2g. It shows the first peak of  $\text{N}_2$ , the second peak

of  $\text{O}_2$ , and the third peak of  $\text{CO}_2$ . As the premixed VOCs were injected into the gas chamber, the dark current patterns in different VOCs (methanol, ethanol, and acetone) were obtained, as shown in Figure 2h–j. The results show that the dark current patterns were dramatically different. The reason for this phenomenon could be the different weight and volume of the VOC molecules. The large volume of the VOC molecules would be a damper to decrease the motion of the small molecules ( $\text{N}_2$  and  $\text{O}_2$ ). Here, gas-phase ions contain air molecules and VOCs that are colliding with each other (few net losses of energy from the collisions due to the elasticity of gas-phase molecules).

**Demonstration of PEIRA.** To increase the sensitivity of the VOC species, the focus area in the gas chamber should be optimized. With a slow adjustment for the maximum irradiation power source in FTIR, the focus sensing area of the mid-IR is shown in Figure S7b. The typical frequency response of the air pressure gases and VOC molecules is shown in Figure 3a. However, the real vibrational mode of the molecules would be affected by the coupling of the strong electric field and the mid-IR during the operation. As shown in Figure S9a, we can observe the response of the mid-IR with/without plasma of the air pressure in the gas measurement chamber. The wavenumber around  $\sim 2400 \text{ cm}^{-1}$  was from  $\text{CO}_2$ , and a coupling effect

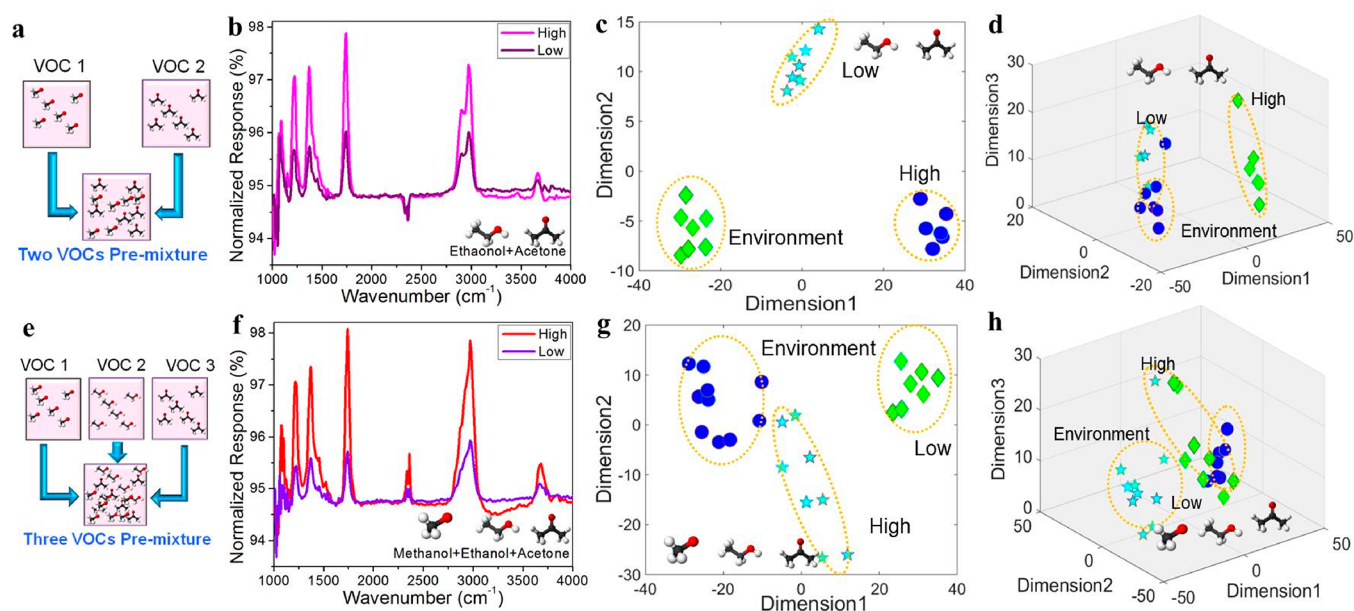


**Figure 5.** Machine-learning-assisted and plasma-enhanced mid-IR methodology for the detection of a mixture of VOCs. (a) VOC premixture chamber with two different VOCs. (b) Response of the mid-IR from two different VOCs in the mixture, ethanol and acetone, and (c) distribution of two different VOCs in 2D and (d) in 3D. (e) VOC premixture chamber with three different VOCs. (f) Response of the mid-IR from three different VOCs in the mixture, methanol, ethanol, and acetone, and (g) the distribution of three different VOCs in 2D and (h) in 3D.

phenomenon was observed (the slight difference between the red curve and the light blue curve). Figure S9b and Figure 3b,c depict the response of the mid-IR with/without any plasma in the gas of methanol, ethanol, and acetone, respectively. The results show that the plasma discharge can increase the response of the mid-IR compared with that without any plasma discharge (strong electric field). PEIRA did affect the response dramatically ( $\sim 1\text{--}3$  times more than the original response without plasma enhancement). The response range was calculated by FTIR in plasma and without plasma. The reason for this enhancement can be explained by the coupling effect of the strong electric field and the mid-IR on the resonance of the molecular structure. It showed wavenumbers of  $\sim 2800$  and  $\sim 3700$   $\text{cm}^{-1}$  for methanol, the wavenumber of  $\sim 2950$   $\text{cm}^{-1}$  for ethanol, and the wavenumber of  $\sim 1800$   $\text{cm}^{-1}$  for acetone, respectively. The four different VOC concentrations of the response of the mid-IR with plasma are shown in Figure 3d–f. A higher concentration of methanol will induce a large value of the peaks around the wavenumber of  $\sim 2800$  and  $\sim 3700$   $\text{cm}^{-1}$ , as shown in Figure 3e. The relationship of methanol concentration versus the response of the mid-IR around the wavenumber can be as shown in Figure 3f. The result shows the almost linear numerical relationship, which can be used to quantify the methanol. Meanwhile, the response of the mid-IR of the ethanol with the plasma discharge is shown in Figure 3g,h, where the wavenumber is  $\sim 2800$   $\text{cm}^{-1}$ . The numerical relationship of the concentration versus response can be calculated as a wavenumber of  $\sim 2950$   $\text{cm}^{-1}$ , as shown in Figure 3i. As for the acetone, the relative information is shown in Figure 3j–l with a wavenumber of  $\sim 1800$   $\text{cm}^{-1}$ . The result shows that all the mentioned VOCs can be well identified by the response around their wavenumbers. Thus, VOC species and their concentrations (methanol, ethanol, and acetone) can be well quantified with both good selectivity and high sensitivity. To identify the methodology for all kinds of VOC gases, three typical VOCs were chosen for the measurement: a VOC with one carbon

(methanol), a VOC with two carbons (ethanol), and a three-carbon VOC (acetone).

**ML-Assisted PEIRA Mixture VOC Detection.** Machine learning is a useful method for better identification than most existing sensing applications. The PCA algorithm in machine learning is one of the standard tools in exploratory data analysis and for model prediction, which can be done by eigenvalue decomposition of data matrix covariance (or correlation). The goal of the PCA is the visualization of the big data for readers to figure out the differences. The 1, 2, and 3 mean the parameters with respect to the direction. The 3D space clusters would contain more information than 2D clusters in PCA. As shown in Figure 4a, the basic logic of PCA is based on the mathematical statistics, where the machine learning method is aimed at the parameters of eigenvalue decomposition of the raw data from the FTIR equipment. Those raw data relating to the mid-IR can be well handled to visualize the VOC species and their concentrations by the PCA algorithm. As shown in Figure S10, all the VOC species and their different concentrations can be observed with a degree of acceptable 2D cluster data dots. The different colors and the shape of marks mean the VOC species at a certain concentration. The results show apparent differences in different concentrations of VOCs. The results also show enough clusters of data dots under the same concentration of a VOC. Figure 4b, d, and f depict three VOCs (methanol, ethanol, and acetone) in 2D space, with significant differences at different concentrations. The results demonstrate the feasibility of the PCA algorithm for VOC detection. To further clarify the difference between them, the various concentrations of VOCs (ethanol, methanol, and acetone) in the modified 3D space are shown in Figure 4c, e, and g, with an apparent cluster of data for the same concentration. The advantages and disadvantages of VOC detection in the existing mechanisms can be found in Table S1 and Table S2.

The premixture chamber was designed for a mixture of the VOCs, as shown in Figure 5a. It was shown that the combinations of VOCs were well premixed with fan rotation

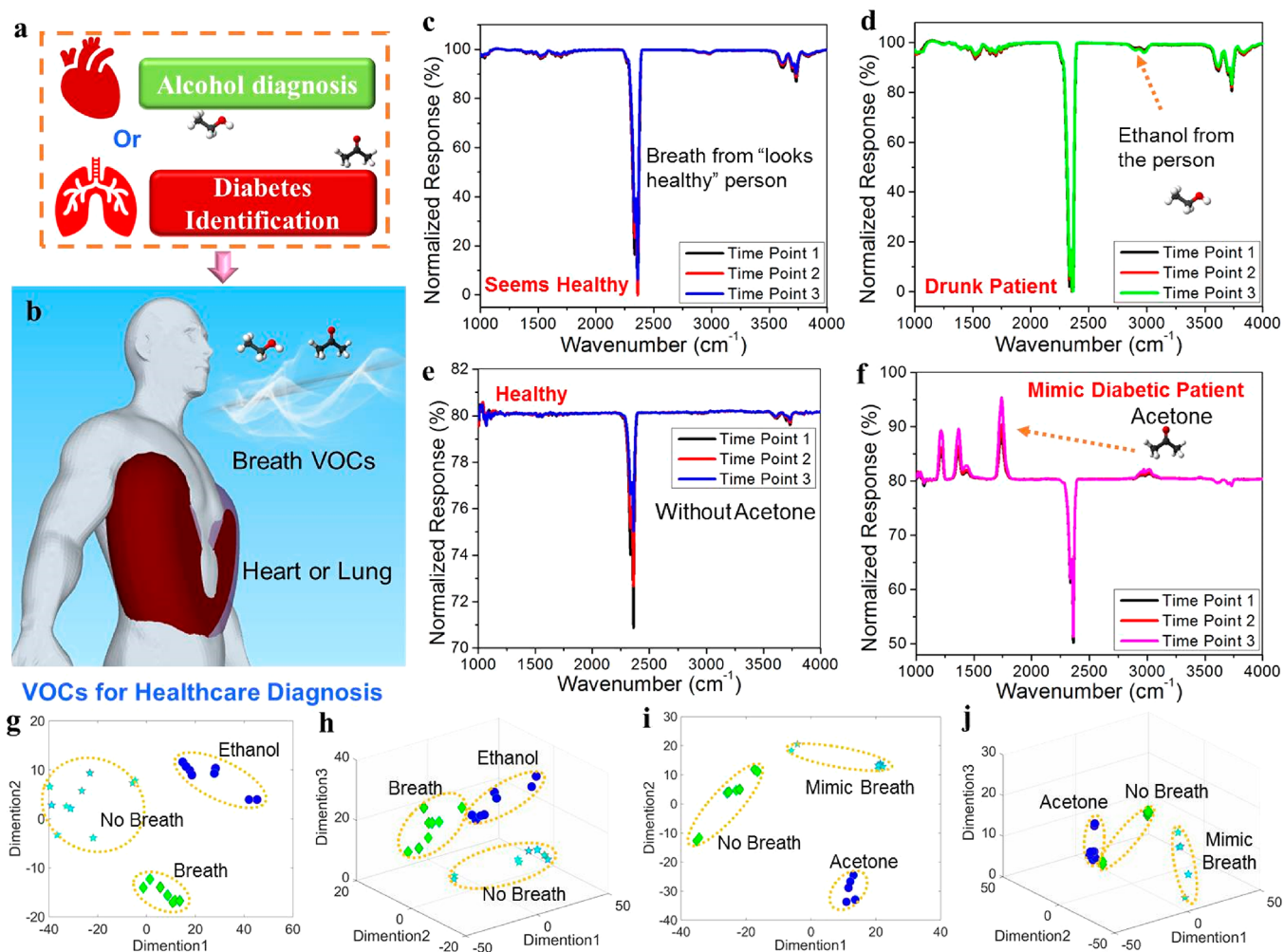


**Figure 6.** Healthcare diagnosis applications using the plasma-enhanced mid-IR for VOCs. (a) Two common illnesses of human beings related to VOCs. (b) 3D schematic diagram of VOCs from a human being's breath for early healthcare diagnosis. (c) Mimic breath by plasma discharge enhancement of the mid-IR from a healthy person; the high peak means CO<sub>2</sub> from the breath, and (d) mimic drunk patient, showing ethanol detection. (e) Mimic of breath from a healthy person and (f) mimic of a diabetic patient; the wavenumber around 1800 cm<sup>-1</sup> demonstrates acetone. (g) Distribution of VOCs in the breath in 2D, ethanol, and (h) in 3D. (i) Distribution of VOCs in the breath in 2D, acetone, and (j) in 3D.

before being injected into the gas measurement chamber. Due to the fixed volume in the premixture chamber, we assumed that each VOC kept its concentrations. To investigate the concentrations of each VOC in a mixture of VOCs, the mid-IR responses of two different concentrations of a variety of VOCs (ethanol and acetone) are shown in Figure 5b. A higher concentration of the mixture of VOCs will induce a more substantial peak around the wavenumbers of ~1800 cm<sup>-1</sup> (acetone) and ~2950 cm<sup>-1</sup> (ethanol). The wavenumbers and the peak value can be used to identify the VOC species and their concentrations, respectively. It was calculated that the "high" and "low" concentrations of the mixture of VOCs were ~2970 ppm + ~1290 ppm and ~1320 ppm + ~860 ppm, respectively. To better explain the visualization relationship of these mixtures of VOCs, the PCA algorithms in 3D and 2D space were adopted, as shown in Figure 5c,d, respectively. The result indicates that the mixture of VOC species and their concentrations can be well-identified based on the cluster of data dots. Moving toward three VOCs (the concentrations of "high" and "low" were ~3630 ppm + ~2970 ppm + ~1290 ppm and ~1100 ppm + ~1320 ppm + ~860 ppm, respectively), as shown in Figure 5e,f,

we can still well distinguish the VOC species and concentrations based on the wavenumbers (methanol of ~3800 cm<sup>-1</sup>, ethanol of ~2950 cm<sup>-1</sup>, and acetone of ~1800 cm<sup>-1</sup>) and the peak values, respectively. The PCAs in 3D and 2D space are shown in Figure 5g,h, respectively. Compared to three VOCs in the mixture, the results showed a much better cluster for two VOCs in the mix. It assumed that the more variable parameters in VOCs decreased the cluster discrimination using PCA. Thus, the machine-learning-assisted method is enough to demonstrate that the system can identify the VOC species and their concentrations by visualization.

**Healthcare Diagnosis Applications.** With the dramatically increasing VOC emissions and healthcare diagnoses for humans, there is a vast need for VOC species detection with good selectivity, fast response, real-time monitoring, and high sensitivity. Figure 6a depicts the common illnesses (alcohol diagnosis and diabetes) associated with long-term exposure to VOCs. Typically, almost no VOCs would be generated from human beings with a good health status. However, when people drink alcohol or are drunk, they will breathe the VOC ethanol. The existing sensors would take at least 3 to 5 min to identify it,

with low efficiency. With the technology of early and fast response in ethanol detection, it would dramatically help police officers find a drinker quickly and avoid transportation accidents. The other example concerns diabetes in early diagnosis; people with this disease breathe acetone molecules due to problems with the stomach, as shown in Figure 6b. The technology using plasma discharge enhancement of mid-IR provides a solution to identify VOC species with fast and on-site detection. The open environment measurement using the mid-IR without/with any plasma can be seen in Figure S11a. As shown in Figure 6c, almost no peaks around the wavenumber of  $\sim 2950\text{ cm}^{-1}$  were demonstrated without any alcohol, but a huge value around a wavenumber of  $\sim 2400\text{ cm}^{-1}$  was present with a large amount of  $\text{CO}_2$  from the breath. Figure 6d and Video S2 depict the detection of ethanol due to a wavenumber of  $\sim 2950\text{ cm}^{-1}$ . The zoom-in curve of a drunk person is shown in Figure S11b. The absolute value of this peak refers to the measured concentrations of ethanol. Figure 6c,d (measurement of human breath) and Figure 6e,f (measurement of a mimic by air flow) were conducted in different scenarios. The former one was observed with a strong response peak of  $\text{CO}_2$  due to the breath from a person, whereas the other one did not. The obvious  $\text{CO}_2$  peak from Figure 6c,d resulted in relatively small ethanol detection from the breath. The small peaks around  $1800$  and  $2900\text{ cm}^{-1}$  from Figure 6c,d were from the unpredictable air from a “healthy looking person” who did the test. The differences from Figure 6c and e were from a “healthy looking person” in breath and the open air conditions, respectively. The wavenumber around  $\sim 2400\text{ cm}^{-1}$  ( $\text{CO}_2$ ) with different directions came from the background calibration. The wavenumber around  $\sim 1800\text{ cm}^{-1}$  demonstrated the VOC acetone, as shown in Figure 6f and Video S3, which gave information about the potential risk of the diabetic. The response value to this peak meant the degree of the severity of the diabetic disease. Furthermore, Figure 6g,h and Figure 6i,j depict three different statuses based on the mid-IR raw data in 2D/3D, respectively, which show significant visualization differences using the machine-learning-assisted method. Thus, the plasma discharge enhancement of the mid-IR provides an ideal solution for the feasibility of early and accurate detection of VOCs in healthcare diagnosis.

## CONCLUSIONS

In summary, we proposed an ML-assisted PEIRA to detect a variety of VOCs in early stage diagnosis, having advantages of fast response, noncontact, good selectivity, real-time monitoring, and high sensitivity. The plasma discharges in the various VOC environments came from a leveraging of the tip–plate electrode configuration, where the voltage with the order of  $\sim\text{kV}$  was from repeatable sliding in the SM-TENG. The enhancement sensing performances of the VOCs were obtained through the coupling of plasma and mid-IR absorption fingerprints. We demonstrated that the various VOCs (methanol, ethanol, and acetone) could be well quantified from the mid-IR spectra within the environment of the mixture of VOCs. Furthermore, the ML-assisted tool was conducted using PCA to visualize the relationships of the different VOC species and concentrations, which demonstrated obvious discrimination according to the right cluster of relevant data. Finally, monitoring of breath from humans showed the feasibility of VOC diagnosis from ML-assisted PEIRA spectroscopy. Our work explores the fundamental phenomenon of plasma–molecule interaction, which indicates the arising of the state-of-the-art PEIRA spectroscopy

technology. We also demonstrate an effective VOC detection by PEIRA for early healthcare diagnosis through ML.

## METHODS

**Fabrication of the SM-TENG.** Two SM-TENGs were fabricated with a contact area of  $10$  and  $49\text{ cm}^2$ , respectively. The SM-TENG contains the bottom pair of plates (dielectric “A” and “C”, both of them are PMMA) and a top movable pair of plates (dielectric “B” and “D”, both of them are FEP). The PMMA dielectric presents positive surface charges when it contacts FEP (negative charges) in operation. The connection wire used in the SM-TENG was a conductive nickel textile. The substrate of the SM-TENG was made of an acrylic plate that was cut by a laser cutting machine. Finally, the entire component was assembled to form the SM-TENG. The FEP film and PTFE film are  $220$  and  $300\text{ }\mu\text{m}$  thick, respectively. The electrode and multiswitches (“on” or “off”) were made of a conductive nickel textile. The reason for choosing this material was its mechanical property with enough mechanical robustness and easy integration to our device. The three states of the SM-TENG are shown in Figure S12: initial, sliding between them, and sliding to a side.

**Characterization.** A programmable electrometer (Keithley model 6514) was used to obtain the  $V_{\text{oc}}$  and  $Q_{\text{oc}}$ , respectively. The output voltage of the measurement was tested by an oscilloscope (Keysight, DSOX3034T) with an internal resistance of  $1$  and  $100\text{ M}\Omega$ . The infrared spectra are provided by a Fourier transformed infrared microscope (Agilent Cary 610 Series) from  $4$  to  $8\text{ }\mu\text{m}$ . The measurement of VOC sensing is conducted at room temperature, and the calibration of the VOC concentration is done with a commercial VOC meter.

**VOC Platform.** Figure S13 in the Supporting Information depicts the setup for VOC detection. The optical images of the SM-TENG and each component are shown in Figure S14. It contains the SM-TENG, the premixture VOC chamber, and the FTIR equipment. The premixed VOC chamber was designed for a mixture of VOC species. The calibration sensor was used to identify the specific concentration of the chosen VOC. The mass flow controllers (MFCs) were connected to the VOC measurement gas chamber. The VOC chamber was sealed well during the measurement and the SM-TENG in operation. The SM-TENG was used to provide the power source for the needle–plate electrode configuration. The oscilloscope was connected to the plate collector to record the dark current response. The computer was used to record the data from FTIR for further machine learning.

## ASSOCIATED CONTENT

### Supporting Information

The Supporting Information is available free of charge at <https://pubs.acs.org/doi/10.1021/acsnano.0c07464>.

Figures S1–S14: response of gas molecules within mid-IR; sliding between two dielectric materials; electrical performance; optical image of the needle–plate; normalized response of the mid-IR; machine-learning-assisted and plasma enhancement; SM-TENG and FTIR in operation (PDF)

Video S1: response of mid-IR (MP4)

Video S2: healthcare diagnosis for a mimic alcohol patient (MP4)

Video S3: healthcare diagnosis for a mimic diabetic using plasma-enhanced mid-IR (MP4)

## AUTHOR INFORMATION

### Corresponding Author

Chengkuo Lee – Department of Electrical and Computer Engineering, National University of Singapore, Singapore 117576, Singapore; Center for Intelligent Sensors and MEMS (CISM) and NUS Graduate School for Integrative Science and Engineering (NGS), National University of Singapore,

Singapore 117576, Singapore; NUS Suzhou Research Institute (NUSRI), Suzhou 215123, People's Republic of China; [orcid.org/0000-0002-8886-3649](https://orcid.org/0000-0002-8886-3649); Email: [elelc@nus.edu.sg](mailto:elelc@nus.edu.sg)

## Authors

**Jianxiang Zhu** – Department of Electrical and Computer Engineering, National University of Singapore, Singapore 117576, Singapore; Center for Intelligent Sensors and MEMS (CISM), National University of Singapore, Singapore 117576, Singapore; NUS Suzhou Research Institute (NUSRI), Suzhou 215123, People's Republic of China; [orcid.org/0000-0002-9172-5255](https://orcid.org/0000-0002-9172-5255)

**Zhihao Ren** – Department of Electrical and Computer Engineering, National University of Singapore, Singapore 117576, Singapore; Center for Intelligent Sensors and MEMS (CISM), National University of Singapore, Singapore 117576, Singapore; NUS Suzhou Research Institute (NUSRI), Suzhou 215123, People's Republic of China

Complete contact information is available at: <https://pubs.acs.org/10.1021/acsnano.0c07464>

## Notes

The authors declare no competing financial interest.

## ACKNOWLEDGMENTS

The authors are grateful for the A\*STAR-NCBR research grant “Chip-Scale MEMS Micro-Spectrometer for Monitoring Harsh Industrial Gases” (R-263-000-C91-305) at the National University of Singapore (NUS), Singapore, the RIE Advanced Manufacturing and Engineering (AME) programmatic grant A18A4b0055 “Nanosystems at the Edge” at NUS, Singapore, and the research grant of CRP-15th (NRF-CRP15-2015-02; R-263-000-C24-281) at NUS, Singapore.

## REFERENCES

- (1) Xie, Z.; Sielemann, S.; Schmidt, H.; Li, F.; Baumbach, J. Determination of Acetone, 2-Butanone, Diethyl Ketone and BTX Using HSCC-UV-IMS. *Anal. Bioanal. Chem.* **2002**, *372*, 606–610.
- (2) Rawal, I.; Sehwat, K.; Kaur, A. Vibrational Spectroscopic Investigations of Ammonia VOC Sensing Mechanism in Polypyrrole Nanostructures. *Vib. Spectrosc.* **2014**, *74*, 64–74.
- (3) Du, Z.; Zhang, S.; Li, J.; Gao, N.; Tong, K. Mid-Infrared Tunable Laser-Based Broadband Fingerprint Absorption Spectroscopy for Trace Gas Sensing: a Review. *Appl. Sci.* **2019**, *9*, 338.
- (4) Zhao, K.; Gu, G.; Zhang, Y.; Zhang, B.; Yang, F.; Zhao, L.; Zheng, M.; Cheng, G.; Du, Z. The Self-Powered VOC Gas Sensor Based on VOC Discharge Induced by Triboelectric Nanogenerator. *Nano Energy* **2018**, *53*, 898–905.
- (5) Teerapanich, P.; Myint, M.; Joseph, C.; Hornyak, G.; Dutta, J. Development and Improvement of Carbon Nanotube-Based Ammonia VOC Sensors Using Ink-Jet Printed Interdigitated Electrodes. *IEEE Trans. Nanotechnol.* **2013**, *12*, 255.
- (6) Rahman, R.; Servati, P. Efficient Analytical Model of Conductivity of CNT/Polymer Composites for Wireless VOC Sensors. *IEEE Trans. Nanotechnol.* **2015**, *14*, 118.
- (7) Consales, M.; Cutolo, A.; Penza, M.; Aversa, P.; Cassano, G.; Giordano, M.; Cusano, A. Carbon Nanotubes Coated Acoustic and Optical VOCs Sensors: towards the Tailoring of the Sensing Performances. *IEEE Trans. Nanotechnol.* **2007**, *6*, 601.
- (8) Gesemann, B.; Wehrspohn, R.; Hackner, A.; Müller, G. Large-Scale Fabrication of Ordered Silicon Nanotip Arrays Used for VOC Ionization in Ion Mobility Spectrometers. *IEEE Trans. Nanotechnol.* **2011**, *10*, 50.

(9) Cho, I.; Kang, K.; Yang, D.; Yun, J.; Park, I. Localized Liquid-Phase Synthesis of Porous SnO<sub>2</sub> Nanotubes on MEMS Platform for Low-Power, High Performance VOC Sensors. *ACS Appl. Mater. Interfaces* **2017**, *9*, 27111–27119.

(10) Cho, M.; Zhu, J.; Kim, H.; Kang, K.; Park, I. Half-Pipe Palladium Nanotube-Based Hydrogen Sensor Using a Suspended Nanofiber Scaffold. *ACS Appl. Mater. Interfaces* **2019**, *11*, 13343–13349.

(11) Matatagui, D.; Sainz-Vidal, A.; Gràcia, I.; Cané, C.; Saniger, J.; Figueras, E. Chemoresistive VOC Sensor Based on ZIF-8/ZIF-67 Nanocrystals. *Sens. Actuators, B* **2018**, *274*, 601–608.

(12) Zhu, J.; Cho, M.; Li, Y.; Cho, I.; Suh, J.; Orbe, D.; Jeong, Y.; Ren, T.; Park, I. Biomimetic Turbinate-Like Artificial Nose for Hydrogen Detection Based on 3D Porous Laser-Induced Graphene. *ACS Appl. Mater. Interfaces* **2019**, *11*, 24386–24394.

(13) Grzebyk, T.; Górecka-Drzazga, A. MEMS Type Ionization Vacuum Sensor. *Sens. Actuators, A* **2016**, *246*, 148–155.

(14) Stark, R.; Schoenbach, K. Direct Current High-Pressure Glow Discharges. *J. Appl. Phys.* **1999**, *85*, 2075.

(15) Reinecke, T.; Kirk, A.; Heptner, A.; Niebuhr, D.; Böttger, S.; Zimmermann, S. A Compact High-Resolution X-Ray Ion Mobility Spectrometer. *Rev. Sci. Instrum.* **2016**, *87*, 053120.

(16) Zheng, X.; Aly, N.; Zhou, Y.; Dupuis, K.; Bilbao, A.; Paurus, V.; Orton, D.; Wilson, R.; Payne, S.; Smith, R.; Baker, E. A Structural Examination and Collision Cross Section Database for over 500 Metabolites and Xenobiotics Using Drift Tube Ion Mobility Spectrometry. *Chem. Sci.* **2017**, *8*, 7724.

(17) Jin, T.; Zhou, J.; Lin, H.; Lin, P. Mid-Infrared Chalcogenide Waveguides for Real-Time and Nondestructive Volatile Organic Compound Detection. *Anal. Chem.* **2019**, *91*, 817–822.

(18) Chang, Y.; Hasan, D.; Dong, B.; Wei, J.; Ma, Y.; Zhou, G.; Ang, K.; Lee, C. All-Dielectric Surface-Enhanced Infrared Absorption-Based VOC Sensor Using Guided Resonance. *ACS Appl. Mater. Interfaces* **2018**, *10*, 38272–38279.

(19) Hasan, D.; Lee, C. Hybrid Metamaterial Absorber Platform for Sensing of VOC Gas at Mid-IR. *Adv. Sci.* **2018**, *5* (1–13), 1700581.

(20) Tuzson, B.; Jagerska, J.; Looser, H.; Graf, M.; Felder, F.; Fill, M.; Tappy, L.; Emmenegger, L. Highly Selective Volatile Organic Compounds Breath Analysis Using a Broadly-Tunable Vertical-External-Cavity Surface-Emitting Laser. *Anal. Chem.* **2017**, *89*, 6377–6383.

(21) Lu, R.; Li, W.; Mizaikoff, B.; Katzir, A.; Raichlin, Y.; Sheng, G.; Yu, H. High-Sensitivity Infrared Attenuated Total Reflectance Sensors for *In Situ* Multicomponent Detection of Volatile Organic Compounds in Water. *Nat. Protoc.* **2016**, *11*, 377–379.

(22) Morrison, P.; Haigis, J. *In Situ* Infrared Measurements of Film and VOC Properties during the Plasma Deposition of Amorphous Hydrogenated Silicon. *J. Vac. Sci. Technol., A* **1993**, *11*, 490.

(23) Cheng, X.; Miao, L.; Song, Y.; Su, Z.; Chen, H.; Chen, X.; Zhang, J.; Zhang, H. High Efficiency Power Management and Charge Boosting Strategy for a Triboelectric Nanogenerator. *Nano Energy* **2017**, *38*, 438–446.

(24) Vasandani, P.; Gattu, B.; Mao, Z.; Jia, W.; Sun, M. Using a Synchronous Switch to Enhance Output Performance of Triboelectric Nanogenerators. *Nano Energy* **2018**, *43*, 210–218.

(25) Xu, L.; Wu, H.; Yao, G.; Chen, L.; Yang, X.; Chen, B.; Huang, X.; Zhong, W.; Chen, X.; Yin, Z.; Wang, Z. Giant Voltage Enhancement via Triboelectric Charge Supplement Channel for Self-Powered Electro-adhesion. *ACS Nano* **2018**, *12*, 10262–10271.

(26) Wang, X.; Song, J.; Liu, J.; Wang, Z. Direct-Current Nanogenerator Driven by Ultrasonic Waves. *Science* **2007**, *316*, 102.

(27) Yang, H.; Pang, Y.; Bu, T.; Liu, W.; Luo, J.; Jiang, D.; Zhang, C.; Wang, Z. Triboelectric Micromotors Actuated by Ultralow Frequency Mechanical Stimuli. *Nat. Commun.* **2019**, *10*, 2309.

(28) Niu, S.; Liu, Y.; Wang, S.; Lin, L.; Zhou, Y.; Hu, Y.; Wang, Z. Theory of Sliding-Mode Triboelectric Nanogenerators. *Adv. Mater.* **2013**, *25*, 6184.

(29) Niu, S.; Wang, Z. Theoretical Systems of Triboelectric Nanogenerators. *Nano Energy* **2015**, *14*, 161.

- (30) He, C.; Han, C.; Gu, G.; Jiang, T.; Chen, B.; Gao, Z.; Wang, Z. Hourglass Triboelectric Nanogenerator as a “Direct Current” Power Source. *Adv. Energy Mater.* **2017**, *7*, 1700644.
- (31) Luo, J.; Xu, L.; Tang, W.; Jiang, T.; Fan, F.; Pang, Y.; Chen, L.; Zhang, Y.; Wang, Z. Direct-Current Triboelectric Nanogenerator Realized by Air Breakdown Induced Ionized Air Channel. *Adv. Energy Mater.* **2018**, *8*, 1800889.
- (32) Liu, D.; Yin, X.; Guo, H.; Zhou, L.; Li, X.; Zhang, C.; Wang, J.; Wang, Z. A Constant Current Triboelectric Nanogenerator Arising from Electrostatic Breakdown. *Sci. Adv.* **2019**, *5*, 6437.
- (33) Zou, H.; Zhang, Y.; Guo, L.; Wang, P.; He, X.; Dai, G.; Zheng, H.; Chen, C.; Wang, A.; Xu, C.; Wang, Z. Quantifying the Triboelectric Series. *Nat. Commun.* **2019**, *10*, 1427.
- (34) Song, W.; Zhu, J.; Gan, B.; Zhao, S.; Wang, H.; Li, C.; Wang, J. Flexible, Stretchable, and Transparent Planar Microsupercapacitors Based on 3D Porous Laser-Induced Graphene. *Small* **2018**, *14*, 1702249.
- (35) Qin, H.; Cheng, G.; Zi, Y.; Gu, G.; Zhang, B.; Shang, W.; Yang, F.; Yang, J.; Du, Z.; Wang, Z. High Energy Storage Efficiency Triboelectric Nanogenerators with Unidirectional Switches and Passive Power Management Circuits. *Adv. Funct. Mater.* **2018**, *28*, 1805216.
- (36) Shi, Q.; Zhang, Z.; Chen, T.; Lee, C. Minimalist and Multifunctional Human Machine Interface (HMI) Using a Flexible Wearable Triboelectric Patch. *Nano Energy* **2019**, *62*, 355–366.
- (37) Xia, K.; Zhu, Z.; Zhang, H.; Du, C.; Wang, R.; Xu, Z. High Output Compound Triboelectric Nanogenerator Based on Paper for Self-Powered Height Sensing System. *IEEE Trans. Nanotechnol.* **2018**, *17*, 1217.
- (38) Zhu, J.; Guo, X.; Meng, D.; Choi, M.; Park, I.; Huang, R.; Song, W. A Flexible Comb Electrode Triboelectric-Electret Nanogenerator with Separated Microfibers for Self-Powered Position, Motion Direction and Acceleration Tracking Sensor. *J. Mater. Chem. A* **2018**, *6*, 16548–16555.
- (39) Qiu, C.; Wu, F.; Shi, Q.; Lee, C.; Yuce, M. Sensors and Control Interface Methods Based on Triboelectric Nanogenerator in IoT Applications. *IEEE Access* **2019**, *7*, 92745–92757.
- (40) Shi, Q.; Lee, C. Self-Powered Bio-inspired Spider-Net-Coding Interface Using Single-Electrode Triboelectric Nanogenerator. *Adv. Sci.* **2019**, *6*, 1900617.
- (41) Yang, J.; Yang, F.; Zhao, L.; Shang, W.; Qin, H.; Wang, S.; Jiang, X.; Cheng, G.; Du, Z. Managing and Optimizing the Output Performances of a Triboelectric Nanogenerator by a Self-Powered Electrostatic Vibrator Switch. *Nano Energy* **2018**, *46*, 220.
- (42) Zhan, Y.; Mei, Y.; Zheng, L. Materials Capability and Device Performance in Flexible Electronics for the Internet of Things. *J. Mater. Chem. C* **2014**, *2*, 1220.
- (43) Chen, H.; Miao, L.; Su, Z.; Song, Y.; Han, M.; Chen, X.; Cheng, X.; Chen, D.; Zhang, H. Fingertip-Inspired Electronic Skin Based on Triboelectric Sliding Sensing and Porous Piezoresistive Pressure Detection. *Nano Energy* **2017**, *40*, 65.
- (44) Wen, X.; Su, Y.; Yang, Y.; Zhang, H.; Wang, Z. Applicability of Triboelectric Generator over a Wide Range of Temperature. *Nano Energy* **2014**, *4*, 150–156.
- (45) Wang, X.; Yang, Y. Effective Energy Storage from a Hybridized Electromagnetic-Triboelectric Nanogenerator. *Nano Energy* **2017**, *32*, 36–41.
- (46) Zhao, K.; Wang, Z.; Yang, Y. Self-Powered Wireless Smart Sensor Node Enabled by an Ultrastable, Highly Efficient, and Superhydrophobic-Surface-Based Triboelectric Nanogenerator. *ACS Nano* **2016**, *10* (9), 9044–9052.
- (47) Yang, Y.; Zhang, H.; Wang, Z. Direct-Current Triboelectric Generator. *Adv. Funct. Mater.* **2014**, *24*, 3745.
- (48) Cheng, G.; Zheng, H.; Yang, F.; Zhao, L.; Zheng, M.; Zhen, M.; Yang, J.; Qin, H.; Du, Z.; Wang, Z. Managing and Maximizing the Output Power of a Triboelectric Nanogenerator by Controlled Tip-Electrode Air-Discharging and Application for UV Sensing. *Nano Energy* **2018**, *44*, 208–216.
- (49) Cheng, J.; Ding, W.; Zi, Y.; Lu, Y.; Ji, L.; Liu, F.; Wu, C.; Wang, Z. Triboelectric Microplasma Powered by Mechanical Stimuli. *Nat. Commun.* **2018**, *9*, 3733.
- (50) Yang, F.; Guo, Z.; Zhao, L.; Shang, W.; Gao, Y.; Zhang, S.; Gu, G.; Zhang, B.; Cui, P.; Cheng, G.; Du, Z. Tuning Oxygen Vacancies and Improving UV Sensing of ZnO Nanowire by Micro-Plasma Powered by a Triboelectric Nanogenerator. *Nano Energy* **2020**, *67*, 104210.
- (51) Wang, Z.; Shi, Y.; Liu, F.; Wang, H.; Liu, X.; Sun, R.; Lu, Y.; Ji, L.; Wang, Z.; Cheng, J. Distributed Mobile Ultraviolet Light Sources Driven by Ambient Mechanical Stimuli. *Nano Energy* **2020**, *74*, 104910.
- (52) Zhao, K.; Gu, G.; Zhang, Y.; Zhang, B.; Yang, F.; Zhao, L.; Zheng, M.; Cheng, G.; Du, Z. The Self-Powered CO<sub>2</sub> Gas Sensor Based on Gas Discharge Induced by Triboelectric Nanogenerator. *Nano Energy* **2018**, *53*, 898–905.
- (53) Liu, F.; Liu, Y.; Lu, Y.; Wang, Z.; Shi, Y.; Ji, L.; Cheng, J. Electrical Analysis of Triboelectric Nanogenerator for High Voltage Applications Exemplified by DBD Microplasma. *Nano Energy* **2019**, *56*, 482–493.
- (54) Li, A.; Zi, Y.; Guo, H.; Wang, Z.; Fernández, F. Triboelectric Nanogenerators for Sensitive Nano-Coulomb Molecular Mass Spectrometry. *Nat. Nanotechnol.* **2017**, *12*, 481–487.
- (55) Zhu, J.; Liu, X.; Shi, Q.; He, T.; Sun, Z.; Guo, X.; Liu, W.; Sulaiman, O.; Dong, B.; Lee, C. Development Trends and Perspectives of Future Sensors and MEMS/NEMS. *Micromachines* **2020**, *11*, 541.
- (56) Wang, Z.; Chen, J.; Lin, L. Progress in Triboelectric Nanogenerators as a New Energy Technology and Self-Powered Sensors. *Energy Environ. Sci.* **2015**, *8*, 2250–2282.
- (57) Zhang, C.; Wang, Z. Tribotronics—A New Field by Coupling Triboelectricity and Semiconductor. *Nano Today* **2016**, *11*, 521.
- (58) Fan, F.; Tian, Z.; Wang, Z. Flexible Triboelectric Generator. *Nano Energy* **2012**, *1*, 328.
- (59) Wang, H.; Wang, J.; He, T.; Li, Z.; Lee, C. Direct Muscle Stimulation Using Diode Amplified Triboelectric Nanogenerators (TENGS). *Nano Energy* **2019**, *63*, 103844.
- (60) He, T.; Wang, H.; Wang, J.; Tian, X.; Wen, F.; Shi, Q.; Ho, J.; Lee, C. Self-Sustainable Wearable Textile Nano-Energy Nano-System (NENS) for Next-Generation Healthcare Applications. *Adv. Sci.* **2019**, *6*, 1901437.
- (61) Zhu, J.; Wang, H.; Zhang, Z.; Ren, Z.; Shi, Q.; Liu, W.; Lee, C. Continuous Direct Current by Charge Transportation for Next-Generation IoT and Real-Time Virtual Reality Applications. *Nano Energy* **2020**, *73*, 104760.
- (62) Wen, F.; Sun, Z.; He, T.; Shi, Q.; Zhu, M.; Zhang, Z.; Li, L.; Zhang, T.; Lee, C. Machine Learning Glove Using Self-Powered Conductive Superhydrophobic Triboelectric Textile for Gesture, Recognition in VR/AR Applications. *Adv. Sci.* **2020**, *7*, 2000261.
- (63) Shi, Q.; Dong, B.; He, T.; Sun, Z.; Zhu, J.; Zhang, Z.; Lee, C. Progress in Wearable Electronics/Photonics – Moving towards the Era of Artificial Intelligence (AI) and Internet of Things (IoT). *InfoMat* **2020**, *2*, 1131–1162.
- (64) Zhu, M.; Sun, Z.; Zhang, Z.; Shi, Q.; He, T.; Liu, H.; Chen, T.; Lee, C. Haptic-Feedback Smart Glove as a Creative Human Machine Interface (HMI) for Virtual/Augmented Reality Applications. *Sci. Adv.* **2020**, *6*, No. eaaz8693.
- (65) Wang, H.; Zhu, J.; He, T.; Zhang, Z.; Lee, C. Programmed-Triboelectric Nanogenerators—a Multi-Switch Regulation Methodology for Energy Manipulation. *Nano Energy* **2020**, *78*, 105241.